DOI: 10.1021/cg100714m

CRYSTAL GROWTH & DESIGN Article

2010, Vol. 10
4823–4830

Growth of Nanosized Calcite through Gas−Solid Carbonation of Nanosized Portlandite under Anisobaric Conditions

G. Montes-Hernandez,*[,†] D. Daval,[‡,§] R. Chiriac,[#] and F. Renard[†,∥]

[†]*CNRS and University Joseph Fourier-Grenoble 1, Laboratoire de Géodynamique des Chaînes Alpines, OSUG/INSU, BP 53, 38042 Grenoble Cedex 9, France,* [‡]*UMR 8538, Ecole Normale Supérieure, 24 Rue Lhomond, 75231 Paris Cedex 5, France,* [§]*Institut de Physique du Globe de Paris, Centre de Recherches sur le Stockage Géologique du CO_2, 4 Place Jussieu, 75005 Paris, France,* [#]*Université de Lyon, Université Lyon 1, Laboratoire des Multimatériaux et Interfaces UMR CNRS 5615, 43 bd du 11 novembre 1918, 69622 Villeurbanne Cedex, France, and* [∥]*Physics of Geological Processes, University of Oslo, NO-0316 Oslo, Norway*

Received May 28, 2010; Revised Manuscript Received September 2, 2010

ABSTRACT: The gas−solid carbonation of nanosized portlandite was experimentally investigated using a static bed reactor under anisobaric conditions. The effects of initial CO_2 pressure (10−40 bar), reaction temperature (30 and 60 °C), and relative humidity were investigated. Three steps of the carbonation process were determined: (1) instantaneous CO_2 mineralization during CO_2 injection period. From 25 to 40 wt % of initial portlandite grains were transformed into calcite during the CO_2 injection period (from 0.9 to 2 min). (2) Fast CO_2 mineralization after gas injection period (< 5 h) followed by (3) a slow CO_2 mineralization until an equilibrium state (< 24 h). The results revealed high efficiency from portlandite-to-calcite transformation (> 95%). For this case, the mineralization of CO_2 does not form a protective carbonate layer around the reacting particles of portlandite as typically observed by other gas−solid carbonation methods. This method could be efficiently performed to produce nanosized calcite. Moreover, the separation of calcite particles from the fluid phase is most simple compared with precipitation methods. A kinetic pseudo-second-order model was satisfactorily used to describe the three CO_2 mineralization steps except for the carbonation reaction initiated at 40 bar. In this latter case, a kinetic pseudo-first-order model was satisfactorily used; indicating that the slow CO_2 mineralization step appears less significant during the carbonation process.

1. Introduction

Basically, carbonate minerals can be formed in natural or artificial environments by three different mechanism pathways and/or conditions: (I) aqueous nucleation-growth in homogeneous or heterogeneous systems (aqueous conditions), for example, the chemical or biogenic formation of carbonates in lakes, oceans, CO_2 storage sites, natural caves; (II) gas−solid carbonation of alkaline minerals (fine particles) in the presence of adsorbed water (water humidity conditions, 0 < water activity < 1), for example, carbonate formation in water-unsaturated soils, in terrestrial or extraterrestrial aerosols; (III) dry gas−solid carbonation of granular/porous materials (dry conditions, water activity ≈ 0), for example, the industrial mineralization, recovery or capture of CO_2 at high temperatures in the presence of alkaline binary oxides (CaO, MgO...) or metastable, nanoparticle alkaline silicates.

Calcium carbonate particles have three crystal polymorphs, namely, calcite, aragonite, and vaterite, which respectively show rhombohedral, needle-like, and spherical morphologies. Calcite belonging to the trigonal class is the most stable phase at room temperature under normal atmospheric conditions, while aragonite and vaterite (e.g., ref 1) belong to the orthorhombic- and hexagonal class, respectively. The later are metastable polymorphs which spontaneously transform into the stable calcite. The specific formation of one of the polymorphs of crystalline calcium carbonate particles depends mainly on the precipitation conditions, such as pH, temperature, and supersaturation. Supersaturation is usually considered to be the main, but nonexclusive, controlling factor.[2] Many experimental studies have been realized on the synthetic precipitation of the various forms of calcium carbonate and the conditions under which these may be produced, including the importance of initial supersaturation, temperature, pH, and hydrodynamics. The effect of impurities and additives has also been extensively studied (e.g., refs 3−16).

The mechanism pathways and/or conditions determine the textural properties (such as average particle size, particle size distribution, crystal morphology, and specific surface area) of the obtained product. For example, in classic aqueous syntheses, the morphology of the precipitated calcite, at typical temperatures of the industrial process (between 30 and 70 °C), is normally the scalenohedral one bounded by the $\{21\bar{1}\}$ form. Synthetic scalenohedral calcite is generally produced through a batch carbonation method. The rhombohedral morphology, bounded by the {104} form, is usually precipitated by using homogeneous systems (i.e., solution−solution interactions) but rarely by the mentioned industrial process. The carbonation of $Ca(OH)_2$ suspension without the addition of additives allows control of the textural properties of calcite precipitates.[17−19] Therefore, the development of new industrial carbonation routes for the production of nanosized calcite particles in the absence of expensive additives and in the absence of liquid media in order to make easier their recovery and use is of great interest. For this reason, we propose the production of nanosized calcite crystals via gas−solid carbonation of powdered portlandite under anisobaric conditions. Whereas most of the previous portlandite carbonation studies were carried out in aqueous media (e.g., refs 17−19) or in wet supercritical CO_2 media (e.g., ref 20), the present synthesis method using

*Corresponding author. E-mail: german.montes-hernandez@obs.ujf-grenoble.fr.

compressed dry CO_2 as the reactant had not yet been experimentally studied, to the best of our knowledge.

The gas−solid carbonation processes using alkaline sorbents are also of growing interest because of their potential to capture CO_2 via noncatalytic exothermic reactions, allowing the selective mineralization of CO_2 from a complex mixture of several gases. Once carbonated, the resulting crystals are then decarbonated to high temperature (the effective value depending on the nature of produced carbonate[21−25]), releasing pure CO_2 by a calcination (or decarbonation) process. This overall carbonation−calcination route allows the recovery of pure CO_2 prior to its injection underground and reuse. Various alkaline sorbents have been proposed to capture and mineralize CO_2 via gas−solid carbonation such as binary oxides (e.g., CaO and MgO), hydroxides (e.g., $Ca(OH)_2$, $Mg(OH)_2$, and NaOH), and metastable powdered silicates (e.g., Li_2SiO_3, Na_2SiO_3, $CaSiO_3$, and $MgSiO_3$).[22−34] For all cases, the CO_2-sorbent reaction is described by the formation of a dense nonporous layer of carbonate minerals (or protective carbonate layer) around the reacting particles, so that carbonation efficiency can be hardly complete (< 80%) (e.g., refs 21, 23, 25, 30, and 34), except for high relative humidity (HR > 95%), small particle size (nanometric scale), and nature of sorbent.[35−37] The formation of a protective carbonate layer produces physically an increase of the volume at the grain scale (expansion or swelling process) or a decrease of porosity (pore closure process) when porous materials are partially carbonated.[25,34,38] With respect to the reaction kinetics, the gas−solid carbonation can be catalyzed by the water activity (or relative humidity) at moderate temperature (< 60 °C) and low CO_2 pressure (< 2 bar), low water activity (< 0.4) ultimately inhibiting the reaction.[39,40] From a mechanistic standpoint, this means that the adsorbed molecular water onto hydrophilic and basic surface sites allows the ion carbonate formation at the gas−solid interfaces followed by the solid carbonate formation around reacting particles. Conversely, for dry gas−solid carbonation (i.e., in the absence of adsorbed water onto reacting particles (water activity ≈ 0)), high temperature (> 120 °C) and preferentially low CO_2 pressure (< 1 bar) are required.[40] In this latter case, the optimized reaction temperature depends directly on the textural properties (e.g., particle size, porosity...) and chemical nature of absorbent.[24,33,34] Note that the reaction mechanism for dry gas−solid carbonation is still a debated question. For instance, some studies have proposed that the atomic excitation at high temperature allows the migration of oxygen atoms from the solid toward adsorbed gaseous CO_2 producing its mineralization into carbonate around the reacting particles.[40] Consequently, the formation of a dense nonporous layer of carbonate minerals around the core of the grains produces a passivation process due to a blocking of intraparticle diffusion of CO_2 through the core of reacting particles.[23]

The gas−solid carbonation has been usually studied at the laboratory scale by using small reactors coupled to thermogravimetric and/or chromatographic measurements.[21,28] Conversely, at the pilot plant scale, fluidized bed reactors have usually been proposed to perform the solid−gas carbonation.[30,31] As previously mentioned, solid−gas carbonation reactions are generally incomplete (< 80%) for both cases due to the formation of a protective carbonate layer around the reacting particles.

The main goal of this study is to demonstrate that a moderate CO_2 pressure makes possible the completion of solid−gas carbonation of nanosized portlandite even with low water activity, whereas identical starting materials were previously demonstrated to exhibit limited, not to say any carbonation at low CO_2 pressure.[40] We show hereafter that this method can be efficiently performed to produce nanosized calcite crystals. Herein, the laboratory experiments on the gas−solid carbonation of powdered portlandite $Ca(OH)_2$ were performed by using a static bed reactor under anisobaric conditions. The effects of initial CO_2 pressure (from 10 to 40 bar), reaction temperature (30 and 60 °C), and two hydration states on solid particles (in situ vacuum drying (P < 10 mbar, T = 110 °C) and without drying (water activity ≈ 0.6) were investigated. The reaction products were characterized by X-ray diffraction (XRD) (including Rietveld refinements of X-ray diffraction patterns), thermogravimetric (TGA), N_2 adsorption (i.e., BET measurements), and microscopic (FESEM and TEM) measurements.

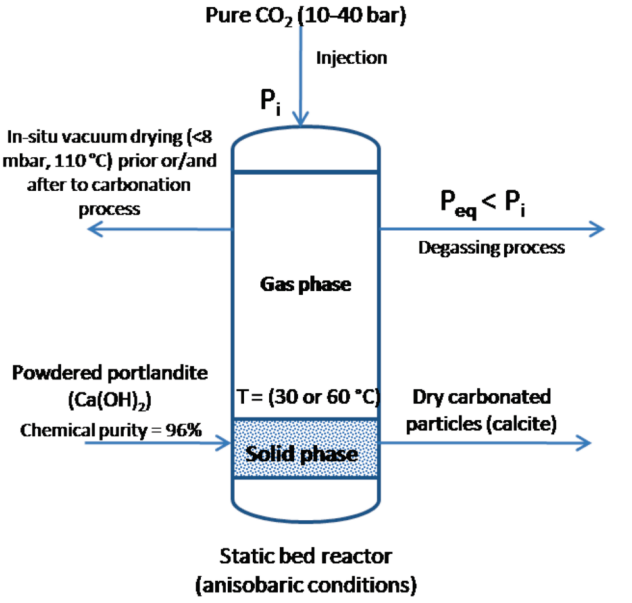

Figure 1. Flow-chart diagram for production of nanosized calcite via gas−solid carbonation of powdered portlandite by using a static bed reactor under anisobaric conditions.

2. Material and Methods

2.1. Growth of Nanosized Calcite. 74.1 g (≈1 mol) of commercial portlandite $Ca(OH)_2$ (provided by Sigma-Aldrich with 96% of chemical purity, about 3% of $CaCO_3$ and 1% of other impurities) were placed in a titanium reactor (Parr autoclave with internal volume of 2 L). The reactor containing solid particles of portlandite was slightly heated to 30 °C using an oven specifically adapted to the reactor. When the system temperature was stabilized, 10, 20, 30, or 40 bar of CO_2 (provided by Linde Gas S. A. with 99.995% of chemical purity) was injected into the static bed reactor. This pressure of CO_2 corresponds to the total initial pressure in the system. At these pressure and temperature (P−T) conditions, the vapor phase consists mainly of CO_2 gas in the ideal state. After CO_2 injection period, from 0.5 to 2 min depending on the initial pressure, the pressure drop was visually monitored on a manometer as a function of time until the CO_2 pressure reached an equilibrium value in this anisobaric gas−solid system (Figure 1). The CO_2 consumption (or CO_2 pressure drop) was monitored as a function of time and directly related to the carbonation kinetics of portlandite at the gas−solid interfaces. However, preliminary tests had revealed an instantaneous significant carbonation of portlandite during the CO_2 injection period. For this reason, complementary experiments were carried out to determine the extent of this instantaneous carbonation. To do so, such carbonation experiments were performed at the same above-mentioned conditions and immediately

stopped after the CO_2 injection period. Herein, the CO_2 gas was immediately removed from the reactor by flash purge down to the atmospheric pressure. The residual CO_2 and in situ produced molecular water ($Ca(OH)_2(s) + CO_2(g) \rightarrow CaCO_3(s) + H_2O$ (v or l)) were removed from the reactor by in situ vacuum drying (< 8 mbar and 110 °C) for 24 h (Figure 1).

At the end of the experiment, that is, after carbonation reaction, flash purge and sometimes in situ vacuum drying, the autoclave was disassembled. The dry solid product was manually recovered, weighed, and stored in plastic flasks for further characterizations (FESEM, TEM, XRD, BET, and TGA).

In order to determine the effect of temperature, a one carbonation experiment was carried out at 60 °C and 20 bar of CO_2 following the same above-mentioned procedure. Finally, to determine the effect of initial adsorbed water onto the reacting particles, the powdered portlandite was in situ dried at 110 °C and < 8 mbar for 24 h using an oven and a vacuum pump specifically adapted to the reactor prior to CO_2 injection.

Note that each carbonation experiment was repeated 2−4 times in order to determine its macroscopic reproducibility.

2.2. Characterization of Solid Particles. Field emission gun scanning electron microscopy (FESEM) was used to characterize the particle size and morphology of crystal faces of carbonated particles, using a Zeiss Ultra 55 microscope with a resolution of around 1 nm at 15 kV. The samples (powders) were previously dispersed by ultrasound in absolute ethanol for 5−10 min. Then, one or two drops of suspension were deposited directly on the metallic supports for SEM observations with fine metal coating of the samples. Additional observations were carried out by transmission electron microscopy (TEM) using a JEOL 2100 (LaB_6) TEM, operating at 200 kV. The sample preparation was similar to that described above: selected carbonated powders were dispersed ultrasonically in pure ethanol; drops of the liquid phase containing the particles in suspension were then subsequently deposited on a carbon-coated copper grid.

Thermogravimetric analyses (TGA) were performed with TGA/SDTA 851^e Mettler Toledo under the following conditions: sample mass of about 20 mg, alumina crucible of 150 μL with a pinhole, heating rate of 20 °C min^{-1}, and air atmosphere of 50 mL min^{-1}. Sample mass loss and associated thermal effects were obtained by TGA/SDTA. In order to integrate the different mass loss steps, the TGA first derivation (mass loss rate) was used. TGA apparatus was calibrated in terms of mass and temperature. Calcium oxalate was used for the sample mass calibration. The melting points of three compounds (indium, aluminum, and copper) obtained from the DTA signals were used for the sample temperature calibration.

The specific surface area of powdered calcite (six samples) was estimated by applying the Brunauer−Emmet−Teller (BET) equation and by using 16.3 $Å^2$ for cross-sectional area of molecular N_2. The N_2 adsorption experiments were performed using a Sorptomatic system (Thermo Electron Corporation).

X-ray diffraction (XRD) data were collected with a Rigaku ultra-X18HFCE Bragg−Brentano diffractometer equipped with a rotating copper anode (Cu Kα radiation). The conditions for generating the X-ray beam were 300 mA and 50 kV. Scans were taken for 2θ ranges from 15 to 90° with 0.01°/s steps.

Rietveld refinement of XRD patterns was carried out with the program Fullprof,[41] following a standard procedure, which can be found in, for example, Montes-Hernandez et al.[42] or Daval et al.[43] Moreover, a specific description of the Rietveld refinement of XRD patterns for this study is given in Supporting Information.

3. Results and Discussion

3.1. Efficiency of Gas−Solid Carbonation of Portlandite. As previously mentioned, a substantial volume of literature has revealed that gas−solid carbonation reactions are generally incomplete (carbonation efficiency <80%) due to the formation of a protective carbonate layer around the reacting particles. In general, at low CO_2 pressure (< 2 bar), the carbonation efficiency of powdered sorbents depends mainly on the particle size, chemical structure, reaction temperature, fluid dynamics, and relative humidity. For portlandite particles, it has been clearly demonstrated that an increase of relative humidity catalyzes the gas−solid carbonation and increases the carbonation efficiency up to 85% at constant low temperature (≈20 °C) and low CO_2 pressure (≈6.5 mbar).[44] The main result of our study consists of the demonstration that the nanosized portlandite can be completely transformed into nanosized calcite via gas−solid carbonation under moderate CO_2 pressure and temperature (Figures 2 and 3). These results can be compared with others from experiments performed on portlandite with identical grain size but at lower CO_2 pressure (e.g., ref 40). Between this previous study[40] and the present one, it is important to notice that all the

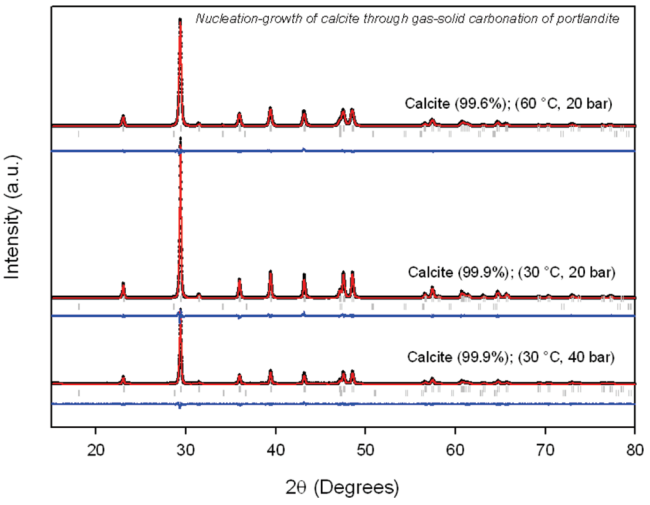

Figure 2. XRD patterns of carbonated particles: Nucleation−growth of calcite particles through gas−solid carbonation of portlandite under three different pressure−temperature conditions. Results of Rietveld refinement of XRD patterns are presented: black points, experimental; red line, Rietveld refined model; blue line, difference; gray lines, position of Bragg peaks (bottom gray lines: portlandite, above gray lines: calcite).

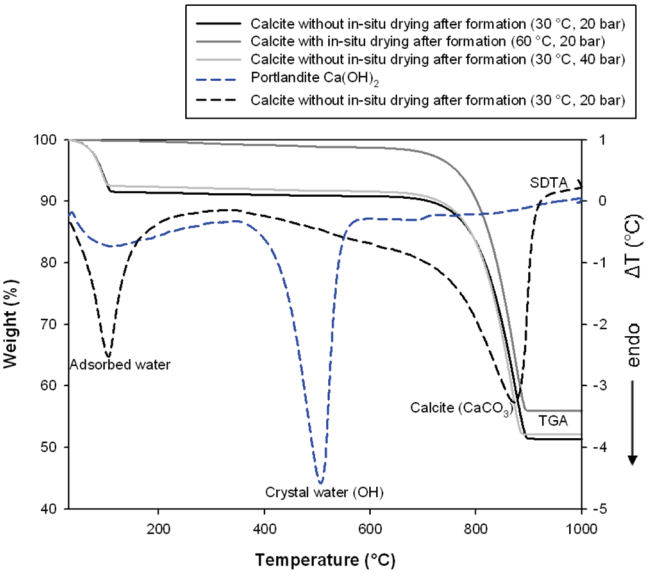

Figure 3. Thermogravimetric curves (TGA) of carbonated particles: Nucleation−growth of calcite particles through gas−solid carbonation of portlandite under three different pressure−temperature conditions. Differential thermal curves (SDTA) of portlandite (reference) and calcite significantly hydrated (adsorbed water).

Table 1. Experimental Conditions and Carbonation Efficiency Determined by Three Independent Methods[a]

					gas−solid carbonation efficiency (wt %)		
exp	CO_2 pressure (bar)	temperature (°C)	$CO_2/Ca(OH)_2$ molar ratio	drying[b]	XRD[c]	TGA[d]	mass balance
1	10	30	0.794	without	57.0	60.0	55.6
2	20	30	1.587	without	99.9	96.1	95.1
3	30	30	2.380	without	nm	nm	95.1
4	40	30	3.174	without	99.9	95.0	95.2
5	20	60	1.444	without	99.5	94.9	96.0
6	20	30	1.587	**with**	99.3	100^{Pnd}	94.4

[a] nm: not measured; Pnd: Portlandite not detected. [b] In situ drying prior to carbonation process (110 °C and < 8 mbar for 24 h). [c] Rietveld refinement of XRD patterns. [d] Thermogravimetric analysis.

physicochemical parameters (other than CO_2 pressure) that impact the carbonation rate and efficiency of portlandite carbonation (i.e., the initial particle size (≈30 nm), the temperature (30 °C), and the water activity (either ≈0 or 0.6)) were kept constant, such that the effect of pressure on the yield and rate of carbonation can be directly addressed in the present study. Our results suggest that the gas−solid carbonation of portlandite particles was enhanced with compressed CO_2. Because the reaction reaches completion for five of the six investigated experimental conditions (see Table 1, where the extent of portlandite carbonation is >95%, except for experiment 1, because CO_2 is the limiting reactant), we conclude that the mineralization of CO_2 does not form a protective carbonate layer around the reacting particles of portlandite. In fact, the formation of a passivating layer would have resulted in a maximum yield of carbonation far lower than 1 (see examples of carbonation reactions leading to passivating ability of secondary coatings in refs 40 and 44). In our experiments, the nucleation−growth of nanosized calcite crystallites were preferentially observed (Figure 4). The results have also revealed that the gas−solid carbonation efficiency with compressed CO_2 was independent of the CO_2 pressure when the $CO_2/Ca(OH)_2$ molar ratio was higher than 1, independent of the reaction temperature (30 and 60 °C) and independent of the initial relative humidity (see Table 1). These new data could increase the interest to use the gas−solid carbonation of portlandite particles with compressed CO_2 (≤40 bar) in order to produce nanosized calcite of high purity. The main advantage compared with precipitation methods is a simple separation of solid product from fluid phase by degassing and conventional drying processes.

3.2. Fitting of Kinetic Macroscopic Data. The CO_2 pressure drop produced by CO_2 consumption during portlandite carbonation process can be directly related to carbonate formation by the following exothermic gas−solid reaction:

$$Ca(OH)_2(s) + CO_2(g) \rightarrow CaCO_3(s) + H_2O(v - or - l) \quad (1)$$

The pressure drop of CO_2 measured as a function of time can be then used to calculate the amount of calcium carbonate formed during this equimolar theoretical reaction. Here, the molar production of calcium carbonate as a function of time ($n_{CaCO_3,t}$) was calculated by

$$n_{CO_2,t} = \frac{(P_0 - P_t)V}{RT} = n_{CaO_3,t} \quad (2)$$

where P_0 represents the initial pressure of CO_2 (10, 20, 30, or 40 bar), P_t stands for the monitored pressure of CO_2 at instant time t (bar), V is the reactor volume occupied with gas (≈2 L), T is the temperature of reaction (303.15 or 333.15 K), and R is the gas constant (0.08314472 L bar/K mol).

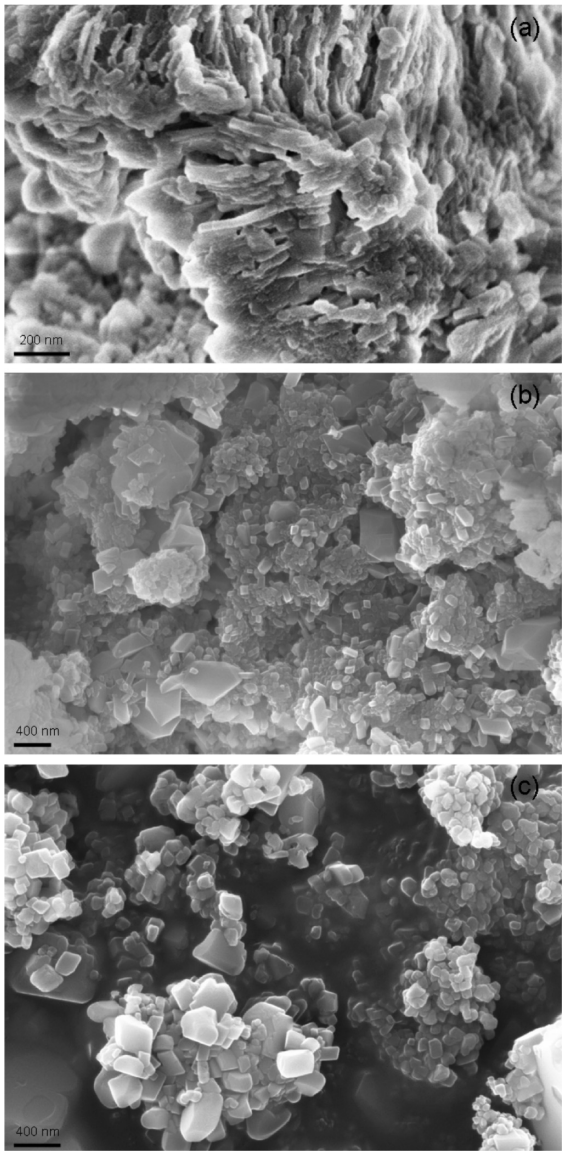

Figure 4. FESEM micrographs obtained via secondary electrons. (a) Platy sub-micrometer grains (sheet forms) of portlandite (reacting particles). Nanosized (< 100 nm) and sub-micrometric (< 1 μm) crystals of calcite formed at 60 °C (b) and 30 °C (c) under anisobaric conditions (initial CO_2 pressure = 20 bar).

The kinetic pseudo-first-order and pseudo-second-order models have been widely used to describe several physicochemical reactions at solid−fluid interfaces such as uptake processes of ions and molecules, photocatalytic oxidation of organic molecules, sorption of vapor water in/on clays, osmotic swelling process of clays, aqueous carbonation of

Table 2. Kinetic and Equilibrium Parameters Determined by Fitting of Experimental Data on the Calcite Nucleation−Growth Using eqs 6 or 7,[a]

exp	model	$n_{CaCO_3,inj}$ (mol)	$n_{CaCO_3,max}$ (mol)	$1/k_{c,1}$ (min)	$t_{1/2}$ (min)	R
30 °C−40 bar (4)	first[b]	0.40 ± 0.009	0.53 ± 0.01	60.24 ± 4.1	na	0.99
30 °C−20 bar (2)	second[c]	0.29 ± 0.02	0.62 ± 0.02	na	68.6 ± 9.9	0.99
30 °C−30 bar (3)	second[c]	0.31 ± 0.02	0.65 ± 0.02	na	34.6 ± 4.5	0.99
60 °C−20 bar (5)	second[c]	0.25 ± 0.02	0.65 ± 0.03	na	83.0 ± 16.0	0.98
dry−30 °C−20 bar (6)	second[c]	0.30 ± 0.02	0.63 ± 0.03	na	70.4 ± 13.5	0.98
30 °C−10 bar (1)[d]	second[c]	0.15 ± 0.03	0.42 ± 0.04	na	166.5 ± 67.8	0.96

[a] na: not applicable. Dry: in-situ drying prior to carbonation process (110 °C and < 8 mbar for 24 h). R: correlation factor. [b] Kinetic pseudo-first-order model. [c] Kinetic pseudo-second-order model. [d] Carbonation experiment where the $CO_2/Ca(OH)_2$ molar ratio < 1.

alkaline minerals and crystal growth processes (e.g., refs 45−51). In the present study, these two kinetic models were also used to describe the kinetic behavior of gas−solid carbonation of portlandite (eq 1) by using the variation of molar CO_2 with time, relating it to calcite formation (eq 2), and assuming a finite equilibration in these closed systems, that is, when the mass transfer was not measurable anymore. The general differential equation to derivate the above cited models can be expressed as

$$\frac{dn_{CaCO_3,t}}{dt} = k_{c,n}(n_{CaCO_3,max} - n_{CaCO_3,t})^n \quad (3)$$

where $k_{c,n}$ is the rate constant of calcite formation, $n_{CaCO_3,max}$ is the maximum molar-amount of calcite at equilibrium, $n_{CaCO_3,t}$ is the molar-amount variation of calcite with time, t (see eq 2), n is a kinetic pseudo-order. For the kinetic pseudo-first-order model, $n = 1$, then, the integrated form of eq 3 for the boundary conditions $t = 0$ to $t = t$ and $n_{CaCO_3,t} = 0$ to $n_{CaCO_3,t} = n_{CaCO_3,t}$, is represented by an exponential relationship:

$$n_{CaCO_3,t} = n_{CaCO_3,max}(1 - \exp(-k_{c,1}t)) \quad (4)$$

For the kinetic pseudo-second-order model ($n = 2$), the integrated form of eqs 3 for the cited above boundary conditions is now represented by a hyperbolic relationship:

$$n_{CaCO_3,t} = \frac{n_{CaCO_3,max}t}{t_{1/2} + t} \text{ where } t_{1/2} = \frac{1}{k_{c,2}n_{CaCO_3,max}} \quad (5)$$

The parameter $t_{1/2}$ represents the duration after which half of the maximum molar-amount of calcite was obtained and is termed "half-carbonation time".

As previously mentioned, the preliminary tests had revealed an instantaneous significant carbonation of portlandite during CO_2 injection period. For this reason, two complementary experiments were carried out in order to determine the quantitative extent of this instantaneous step. Herein, the calcite instantaneous-formation during CO_2 injection period ($n_{CaCO_3,inj}$) was experimentally determined by mass balance methods (TGA and Rietveld refinement of XRD patterns). This experimental parameter can be incorporated into eqs 4 and 5in order to obtain a more realistic kinetic behavior of calcite formation during carbonation process of portlandite. Then, the corrected equations can be finally expressed as

$$n_{CaCO_3,t} = n_{CaCO_3,inj} + n_{CaCO_3,max}(1 - \exp(-k_{c,1}t)) \quad (6)$$

for the kinetic pseudo-first-order model, and

$$n_{CaCO_3,t} = n_{CaCO_3,inj} + \frac{n_{CaCO_3,max}t}{t_{1/2} + t} \quad (7)$$

for the kinetic pseudo-second-order model.

The fitting of kinetic data ($n_{CaCO_3,t}$ vs t) by using eqs 6 or 7 allows the estimation of kinetic and equilibrium parameters.

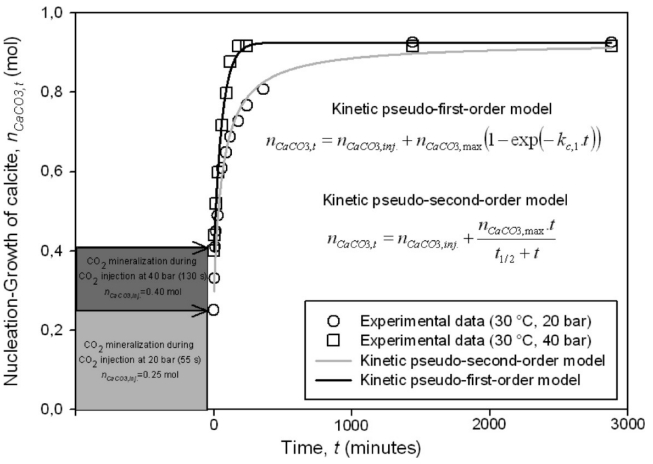

Figure 5. Kinetic behavior of nucleation−growth of calcite through gas−solid carbonation of portlandite under anisobaric conditions at 30 °C.

A nonlinear regression by the least-squares method was performed. In Figure 5, the experimental data and fitting curves are reported for two of the six investigated conditions (note that the fitting parameters and the correlation factor values for the entire data set are summarized in the Table 2). In general, these results have demonstrated three steps of the carbonation process or calcite nucleation−growth via gas−solid carbonation: (I) Instantaneous CO_2 mineralization during CO_2 injection period. From 25 to 40% of initial portlandite was transformed into calcite during the CO_2 injection period (from 0.9 to 2 min). (II) Fast CO_2 mineralization after gas injection period (< 5 h) followed by (III) a slow CO_2 mineralization until an equilibrium state (< 24 h). At this equilibrium state, the estimation of the maximum molar-amount of calcite added to instantaneous CO_2 mineralization ($n_{CaCO_3,max}$ + $n_{CaCO_3,inj}$) are in agreement with thermogravimetric (TGA) and diffractometric (XRD) measurements. In summary, a kinetic pseudo-second-order model was satisfactory used to describe these three CO_2 mineralization steps except for the carbonation reaction initiated at 40 bar. In this latter case, a kinetic pseudo-first-order model was satisfactory used; this indicates that the slow CO_2 mineralization step (or slow mass transfer step) appears less significant during the carbonation process (Figure 5). The slow CO_2 mineralization step observed in our experiments (when initial CO_2 pressure < 40) can be due to the continuous consumption of CO_2 "manifested by a continuous pressure drop" (anisobaric conditions) until an equilibrium state in this closed system. Moreover, the water formation from carbonation reaction (see eq 1) could result in a local acidification process at the carbonate−water−CO_2 interfaces, leading to complex dissolution−reprecitation features, slowing down in turn the global carbonation rate of portlandite.

Table 3. Results of BET Measurements and the Average Particle Size Deduced from Specific Surface and Rietveld Refinement of XRD Patterns[a]

exp	pCO_2(bar)	temperature (°C)	$CO_2/Ca(OH)_2$ molar ratio	drying[b]	S_{BET} (m^2/g)	D (nm)	r_e (nm)	l_{TEM} (nm)
1	10	30	0.794[c]	without	9.2	250	29	nm
2	20	30	1.587	without	7.0	310	94	nm
3	30	30	2.380	without	nm	na	nd	nm
4	40	30	3.174	without	9.4	230	102	nm
5	20	60	1.444	without	8.1	270	44	nm
6	20	30	1.587	**with**	5.5	400	95	122[d]
		starting material (portlandite)			15.3	170	29	nm

[a] nm: not measured; na: not applicable; nd: not determined; S_{BET}: specific surface area of starting and carbonated materials; D: average particle size of starting and carbonated materials estimated by assuming all the particles have the same spherical/cubic shape and size; r_e: coherent domain average size of calcite (at the macroscopic equilibrium "after 24 h of reaction") and portlandite (starting material) determined by Rietveld refinement of XRD patterns; l_{TEM}: average particle size of calcite manually measured from TEM micrograph (see Figure 6). [b] In situ drying prior to carbonation process (110 °C and < 8 mbar for 24 h). [c] Incomplete reaction (i.e., mixture calcite (0.58) − portlandite (0.42)). [d] Average value considering 20 representative crystals (see Figure 6).

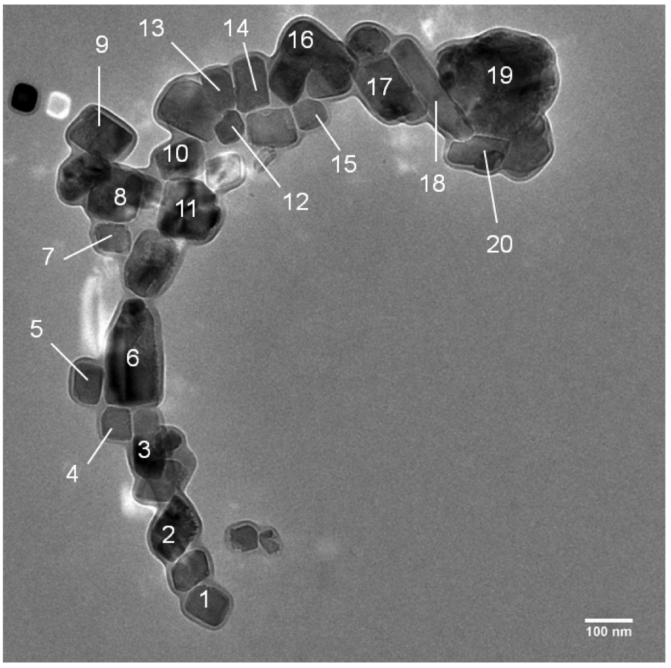

Crystal	Length (nm)
1	99.7
2	121.1
3	121.6
4	69.9
5	100.0
6	198.3
7	68.4
8	115.7
9	121.2
10	97.7
11	123.4
12	60.3
13	92.8
14	108.5
15	67.7
16	151.3
17	158.2
18	233.5
19	231.4
20	107.5
average	122.4
std dev	50.1

Figure 6. TEM micrograph showing nanosized (< 100 nm) and sub-micrometric (< 1 μm) calcite crystals (concerning experiment 6).

A final comment can be made with respect to the kinetic parameters determined in the present study. As one can note, the fitted/experimental parameters (e.g., $n_{CaCO_3,inj}$; $t_{1/2}$) are strongly correlated with the initial CO_2 pressure. Basically, the higher the initial pressure, the faster the reaction, which is qualitatively consistent with the idea that the rate-limiting step is rather more related to the CO_2 pressure itself than to surface coverage limitations. Although more data would be required to accurately link the parameters $n_{CaCO_3,inj}$ and $t_{1/2}$ to the initial CO_2 pressure, here we showed results which make us envisage that for a given experimental configuration, a simple and predictive model could be built by using the initial CO_2 pressure as the only entry parameter to foresee the carbonation rates.

3.3. Features of Reaction Products and Variation of Average Particle Size Related to Crystal Growth Process of Calcite. The BET measurements have revealed a high specific surface area (see Table 3) compared with typical values of powdered calcite. These values lead to a sub-micrometric average particle size for all carbonated samples (from 230 to 400 nm) assuming all the particles to have the same spherical/cubic shape and size. This simple calculation on the average particle size deduced from specific surface area is significantly in disagreement with coherent domain average size. This latter size parameter is determined by Rietveld refinement of XRD patterns (values also reported in Table 3). To explain this discrepancy, a carbonated sample (concerning experiment 6) was imaged by transmission electron microscopy (TEM) (see Figure 6). Here, the average particle size considering 20 representative calcite crystals is about 122 nm. This size value is clearly in agreement with coherent domain average size determined by Rietveld refinement of XRD patterns. On the basis of this specific result, the significant discrepancy between BET and XRD measurements (reported in Table 3) can be explained in terms of aggregation state and assuming the presence of closed pores into aggregates, that is, pores in aggregates not accessible by N_2 during conventional BET measurements.

Finally, the average particle size of portlandite and calcite determined by Rietveld refinement of XRD patterns were reported in Figure 7. In addition to the final size of calcite crystals at the end of the reaction, powders were recovered and analyzed at intermediate stages of the carbonation process in order to give some insights into the crystal growth process. Several comments can be established from Figure 7. First, it can be noticed that the main factor controlling the final size of calcite crystals is temperature: whereas the final calcite grain size for experiments 2, 4, and 6 run at 30 °C are

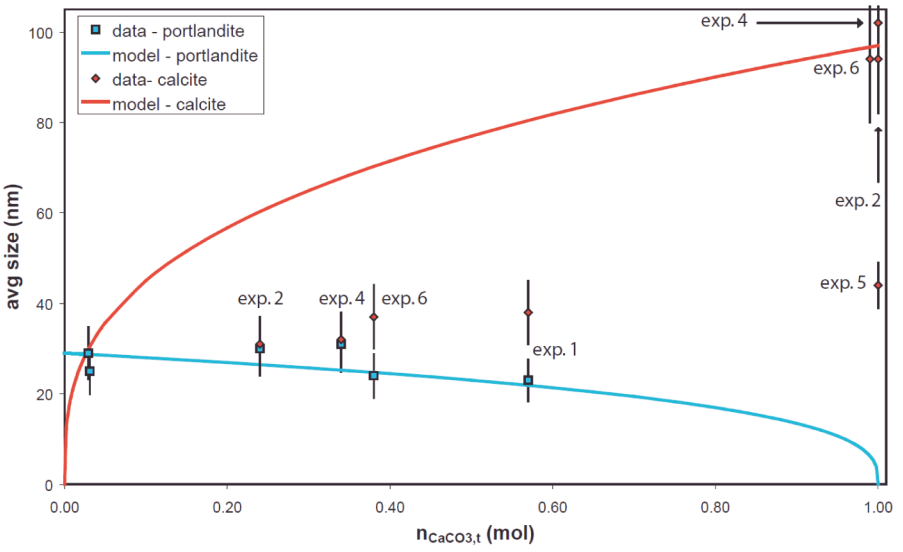

Figure 7. Average coherent domain size of portlandite (squares) and calcite (diamonds) particles as a function of the molar-amount of calcite formed. The solid blue line represents the expected evolution of the size of portlandite particles following a shrinking core model and an initial size of particles of 29 nm. A symmetric model for the homogeneous growth of calcite crystals cannot explain the results obtained with calcite (solid red line).

very similar (close to 100 nm, this value being in excellent agreement with the TEM observations), the final grain size of calcite is 44 nm for experiment 5 run at 60 °C. Conversely, for a given temperature, the effects of initial pressure and relative humidity are not significant (see the data points corresponding to the equilibrium state for experiments 2, 4, and 6). The main conclusion of this observation is that the maximal extents of carbonation are independent of the calcite grain size, which is an additional argument in favor of a process that is not transport-limited (see e.g., ref 52, where the passivating ability of carbonate coatings is proposed to be critically linked to the average size of crystallites).

Considering that the size of calcite crystallites at equilibrium are roughly equivalent in experiments 2, 4 and 6, it can be supposed that the evolution of the size of calcite crystals as a function of the extent of carbonation is similar during each one of these three experiments (the same assumption could hold for the evolution of portlandite crystallites).

For the sake of simplicity, if we use the common approach which assumes that both calcite and portlandite crystals consist of spherical particles, then the size of the crystallites can be determined at any time (t_i) following:

$$d_{t=t_i} = \left(\frac{6}{\pi} \times \frac{m_{t=t_i}}{\rho}\right)^{1/3} \tag{8}$$

where $d_{t=t_i}$ and $m_{t=t_i}$ are respectively the diameter and mass of a given particle at t_i, ρ being its specific gravity. Equation 8 can be rewritten specifically at $t_i = 0$ for portlandite and at $t_i = t_{eq}$ for calcite (i.e., the time required to reach equilibrium), which yields, after rearrangement:

$$\left(\frac{6}{\pi\rho}\right)^{1/3} = \frac{d_{t=0}^{\text{portlandite}}}{\left(m_{t=0}^{\text{portlandite}}\right)^{1/3}} \tag{9a}$$

and

$$\left(\frac{6}{\pi\rho}\right)^{1/3} = \frac{d_{t=t_{eq}}^{\text{calcite}}}{\left(m_{t=t_{eq}}^{\text{calcite}}\right)^{1/3}} \tag{9b}$$

for portlandite and calcite respectively. Substituting $(6/\pi\rho)^{1/3}$ in eq 8 by its expression taken either from 9a or 9b yields:

$$d_{t=t_i}^{\text{portlandite}} = d_{t=0}^{\text{portlandite}} \left(\frac{m_{t=t_i}^{\text{portlandite}}}{m_{t=0}^{\text{portlandite}}}\right)^{1/3} \tag{10a}$$

and

$$d_{t=t_i}^{\text{calcite}} = d_{t=t_{eq}}^{\text{calcite}} \left(\frac{m_{t=t_i}^{\text{calcite}}}{m_{t=t_{eq}}^{\text{calcite}}}\right)^{1/3} \tag{10b}$$

Finally, because the experiments were run with a starting amount of ≈1 mol of portlandite, and considering the stoichiometry of the carbonation reaction, one can easily show that the two equations above can be rewritten as a function of $n_{CaCO_3,t}$ following:

$$d_{t=t_i}^{\text{portlandite}} = d_{t=0}^{\text{portlandite}} (1 - n_{CaCO_3,t})^{1/3} \tag{11a}$$

and

$$d_{t=t_i}^{\text{calcite}} = d_{t=0}^{\text{calcite}} (n_{CaCO3,t})^{1/3} \tag{11b}$$

The curves corresponding to these models were drawn on Figure 7 (light blue and red lines for portlandite and calcite, respectively), taking an initial particle size of 29 nm for portlandite and a final particle size of 97 nm for calcite (these boundary conditions being determined by the results of Rietveld refinements of XRD patterns). As one can see, the evolution of the average size of portlandite crystallites, which could have seemed surprising as it only tends to decrease slightly as a function of the extent of carbonation, is indeed in fair agreement with a basic shrinking particle model. Conversely, this simple homogeneous model cannot account for the evolution of calcite growth as a function of carbonation extent (Figure 7, comparison between red solid line and red diamonds). If one was to expect "big" calcite crystals of ≈100 nm at the end of the reaction, then the intermediate size of the corresponding crystals for $0.2 < n_{CaCO_3,t} < 0.6$ should be comprised between 57 and 82 nm, whereas they actually range between 31 and 38 nm. The only way to obtain crystals 100-nm-thick from seeds 35-nm-thick

is to dissolve parts of these seeds, such that the released amount of Ca^{2+} and HCO_3^- species can precipitate on some of the bigger crystals, whereas the smallest shrink (i.e., following an Ostwald ripening-like path). Thus, as previously discussed, these preliminary results could reflect a complex precipitation−dissolution process of calcite crystallites at large extent of carbonation, as water is released from portlandite (see eq 1). Even though more data would be necessary to confirm such a process, which will be the main concern of an upcoming study, here is an interesting illustration of some powerful information which can be retrieved from Rietveld refinement of XRD patterns.

4. Conclusion

In summary, we demonstrated that nanosized portlandite can be completely transformed into nanosized calcite (< 100 nm) via gas−solid carbonation under moderate CO_2 pressure (< 40 bar) and low temperature (< 60 °C). For this case, the mineralization of CO_2 does not form a protective carbonate layer around the reacting particles of portlandite as typically observed by other carbonation methods. This method could be efficiently performed to produce nanosized calcite with high potential for industrial (e.g., filler in papermaking industry and printing inks, antacid tablets, adsorbents...) applications. Moreover, the separation of solid product from the fluid phase is simpler than in precipitation methods.

Acknowledgment. The authors are grateful to French National Center for Scientific Research (CNRS) and University Joseph Fourier (UJF) in Grenoble for providing the financial support. Nathaniel Findling (ENS, Paris) is acknowledged for his help with the acquisition of X-ray diffractograms.

Supporting Information Available: Specific comments for Rietveld refinements. This material is available free of charge via the Internet at http://pubs.acs.org.

References

(1) Wang, J.; Becker, U. *Am. Mineral.* **2009**, *94*, 380.
(2) Han, Y. S.; Hadiko, G.; Fuji, M.; Takahashi, M. *J. Cryst. Growth* **2005**, *276*, 541.
(3) Moore, L.; Hopwood, J. D.; Davey, R. J. *J. Cryst. Growth* **2004**, *261*, 93.
(4) Westin, K. J.; Rasmuson, A. C. *J. Colloids Interface Sci.* **2005**, *282*, 370.
(5) Tsuno, H.; Kagi, H.; Akagi, T. *Bull. Chem. Soc. Jpn.* **2001**, *74*, 479.
(6) Fujita, Y.; Redden, G. D.; Ingram, J.; Cortez, M. M.; Ferris, G.; Smith, R. W. *Geochem. Cosmochem. Acta* **2004**, *68*, 3261.
(7) Freij, S. J.; Godelitsas, A.; Putnis, A. *J. Cryst. Growth* **2005**, *273*, 535.
(8) Gower, L. A.; Tirrell, D. A. *J. Cryst. Growth* **1998**, *191*, 153.
(9) Jonasson, R. G.; Rispler, K.; Wiwchar, B.; Gunter, W. D. *Chem. Geol.* **1996**, *132*, 215.
(10) Chrissanthopoulos, A.; Tzanetos, N. P.; Andreopoulou, A. K.; Kallitsis, J.; Dalas, E. *J. Cryst. Growth* **2005**, *280*, 594.
(11) Menadakis, M.; Maroulis, G.; Koutsoukos, P. G. *Comput. Mater. Sci.* **2007**, *38*, 522.
(12) Dousi, E.; Kallitsis, J.; Chrisssanthopoulos, A.; Mangood, A. H.; Dalas, E. *J. Cryst. Growth* **2003**, *253*, 496.
(13) Pastero, L.; Costa, E.; Alessandria, B.; Rubbo, M.; Aquilano, D. *J. Cryst. Growth* **2003**, *247*, 472.
(14) Lee, Y. J.; Reeder, R. *Geochem.Cosmochem. A.* **2006**, *70*, 2253.
(15) Temmam, M.; Paquette, J.; Vali, H. *Geochem. Cosmochem. A.* **2000**, *64*, 2417.
(16) Dalas, E.; Chalias, A.; Gatos, D.; Barlos, K. *J. Colloids Interface Sci.* **2006**, *300*, 536.
(17) Domingo, C.; García-Carmona, J.; Loste, E.; Fanovich, A.; Fraile, J.; Gómez-Morales, J. *J. Cryst. Growth* **2004**, *271*, 268.
(18) García-Carmona, J.; Gómez Morales, J.; Rodríguez Clemente, R. *J. Cryst. Growth* **2003**, *249*, 561.
(19) García-Carmona, J.; Gómez Morales, J.; Rodríguez Clemente, R. *J. Colloid Interface Sci.* **2003**, *261*, 434.
(20) Gu, D. W.; Bousfield, C. P.; Tripp, C. P. *J. Mater. Chem.* **2006**, *16*, 3312.
(21) Prigiobbe, V.; Polettini, A.; Baciocchi, R. *Chem. Eng. J.* **2009**, *148*, 270.
(22) Shtepenko, O. L.; Hills, C. D.; Coleman, N. J.; Brough, A. *Environ. Sci. Technol.* **2005**, *39*, 345.
(23) Stendardo, S.; Foscolo, P. U. *Chem. Eng. Sci.* **2009**, *64*, 2343.
(24) Zevenhoven, R.; Teir, S.; Eloneva, S. *Energy* **2008**, *33*, 362.
(25) Sun, P.; Grace, J. R.; Lim, C. J.; Anthony, E. J. *Chem. Eng. Sci.* **2008**, *63*, 57.
(26) Gauer, C.; Heschel, W. *J. Mater. Sci.* **2006**, *41*, 2405.
(27) Essaki, K.; Kato, M.; Uemoto, H. *J. Mater. Sci.* **2005**, *21*, 5017.
(28) Regnault, O.; Lagneau, V.; Schneider, H. *Chem. Geol.* **2009**, *265*, 113.
(29) Purnell, P.; Seneviratne, A. M.G.; Short, N. R.; Page, C. L. *Composite: Part A* **2003**, *34*, 1105.
(30) Huntzinger, D. N .; Gierke, J. S.; Kawatra, S. K.; Eisele, T. C.; Sutter, L. L. *Environ. Sci. Technol.* **2009**, *43*, 1986.
(31) Reddy, K.; Argyle, M; Attili, V.; Jackson, R.; Fahlsing, P.; Bhattachryya, P.; John, S. *Environ. Sci. Technol.* **2010** In revision.
(32) Lanas, J.; Alvarez, J. I. *Thermochim. Acta* **2004**, *423*, 1.
(33) Wang, C.; Jia, L.; Tan, Y.; Anthony, E. J. *Fuel* **2008**, *87*, 1108.
(34) Fernandez Bertos, M.; Simons, S. J. R.; Hills, C. D.; Carey, P. J. *J. Hazard. Mater.* **2004**, *B112*, 193.
(35) Dheilly, R. M.; Tudo, J.; Sebai, Y.; Queneudec, M. *Construction Building Mater.* **2002**, *16*, 155.
(36) Zeman, F. *Int. J. Greenhouse Gas Control* **2008**, *2*, 203.
(37) Seo, Y.; Jo., S.-H.; Ryu, C. K.; Yi, C.-K. *Chemosphere* **2007**, *69*, 712.
(38) Chen, M.; Wang, N.; Yu, J.; Yamaguchi, A. *J. European Ceram. Soc.* **2007**, *27*, 1953.
(39) Rao, A.; Anthony, E. J.; Manovic, V. *Fuel* **2008**, *87*, 1927.
(40) Montes-Hernandez, G.; Pommerol, A.; Renard, F.; Beck, P.; Quirico, E.; Brissaud, O. *Chem. Eng. J.* **2010**, *161*, 250.
(41) Rodriguez-Carvajal, J. 2010, http://www.ill.eu/sites/fullprof/php/tutorials.html
(42) Montes-Hernandez, G.; Fernandez-Martinez, A.; Charlet, L.; Tisserand, D.; Renard, F. *J. Cryst. Growth* **2008**, *310*, 2946.
(43) Daval, D.; Martinez, I.; Guigner, J.-M.; Hellmann, R.; Corvisier, J.; Findling, N.; Dominici, C.; Goffé, B.; Guyot, F. *Am. Mineral.* **2009**, *94*, 1707.
(44) Beruto, D. T.; Botter, R. *J. Eur. Ceramic Soc.* **2000**, *20*, 497.
(45) Ho, Y.-S. *J. Hazard. Mater.* **2006**, *136*, 681.
(46) Ho, Y.-S.; McKay, G. **1999**, *34*, 451.
(47) Montes-H, G.; Geraud, Y. *Colloids Surf., A* **2004**, *235*, 17.
(48) Montes-H, G. *J. Colloids Int. Sci.* **2005**, *284*, 271.
(49) Montes-Hernandez, G.; Rihs, S. *J. Colloids Int. Sci.* **2006**, *299*, 49.
(50) Montes-Hernandez, G.; Renard, F.; Geffroy, N.; Charlet, L.; Pironon, J. *J. Cryst. Growth* **2007**, *308*, 228.
(51) Montes-Hernandez, G.; Concha-Lozano, N.; Renard, F.; Quirico *J. Hazard. Mater.* **2009**, *166*, 788.
(52) Daval, D.; Martinez, I.; Corvisier, J.; Findling, N.; Goffé, B.; Guyot, F. *Chem. Geol.* **2009**, *265*, 63.